

From high- T_c to low- T_c : Multi-orbital effects in transition metal oxides

Michael Klett,^{1,*} Tilman Schwemmer,^{1,*} Sebastian Wolf,² Xianxin Wu,^{3,4} David Riegler,¹ Andreas Dittmaier,¹ Domenico Di Sante,¹ Gang Li,^{5,6} Werner Hanke,¹ Stephan Rachel,^{2,†} and Ronny Thomale^{1,‡}

¹*Institute for Theoretical Physics, University of Wuerzburg, D-97074 Wuerzburg, Germany*

²*School of Physics, University of Melbourne, Parkville, VIC 3010, Australia*

³*Max-Planck-Institut für Festkörperforschung, Heisenbergstrasse 1, D-70569 Stuttgart, Germany*

⁴*Beijing National Laboratory for Condensed Matter Physics,*

⁵*School of Physical Science and Technology, ShanghaiTech University, Shanghai 201210, China*

⁶*ShanghaiTech Laboratory for Topological Physics,
ShanghaiTech University, Shanghai 201210, China*

(Dated: December 30, 2021)

Despite the structural resemblance of certain cuprate and nickelate parent compounds there is a striking spread of T_c among such transition metal oxide superconductors. We adopt a minimal two-orbital e_g model which covers cuprates and nickelate heterostructures in different parametric limits, and analyse its superconducting instabilities. The joint consideration of interactions, doping, Fermiology, and in particular the e_g orbital splitting allows us to explain the strongly differing pairing propensities in cuprate and nickelate superconductors.

Introduction.—High-temperature unconventional superconductivity, as discovered in copper oxides in 1986 [1], has ever since decisively framed the landscape of research in condensed matter physics. In particular, many trends of T_c as a function of tunable system parameters have been investigated. The hope is to identify a way to tune the cuprates just enough to approach room temperature, and hence render them, or another class of unconventional superconductors, technologically viable [2, 3]. Initially, the rather accurate single-orbital one-band Hubbard model description was assumed to be an advantageous, and hence already T_c optimized, feature of the copper oxide superconductors. Due to the Jahn-Teller effect, the apical oxygen distance to the CuO_2 planes is elongated, and thus ensures a splitting of the e_g orbitals such that the $3d^9$ configuration of Cu yields a nearly exclusive hole population of the $3d_{x^2-y^2}$ orbital [4].

Research on unconventional superconductivity over the past two decades indicates that this picture, in its generality, needs revision [5]. While orbital fluctuations may be detrimental to high- T_c , multi-orbital systems can also yield beneficial effects for unconventional superconductivity, such as the multi-pocket Fermiology of iron-based superconductors [6, 7]. Interpreting the single-band cuprates as the nucleus for high- T_c superconductivity, the addition of multi-orbital character can thus take different turns. Nickelate thin film heterostructures such as $\text{LaNiO}_3/\text{LaAlO}_3$, whose electronic structure is suggested to be analogous to the high- T_c cuprate compounds [8, 9], only show a T_c as low as 3 K [10]. This might hint at the detrimental effect of orbital fluctuations, which would be in line with a precise analysis of the impact of interactions on the orbital polarization [11]. We call this a low- T_c instance of multi-orbital effects. To the contrary, $\text{Ba}_2\text{CuO}_{3+\delta}$, where e_g orbital fluctuations are likewise expected to be as prominently present as in LaNiO_3 heterostructures, reaches a T_c as high as 70 K [12], which

we highlight as a high- T_c instance. Note that all aforementioned material examples of transition metal oxide superconductors are characterized by the e_g orbitals of the transition metal atom at low energies, albeit for different orbital fillings (Ni $3d^7$ versus Cu $3d^9$), doping levels, and Fermi surface topologies (Fermiologies). Adopting the view from a generalized e_g two-orbital octahedral oxide setting, $\text{Ba}_2\text{CuO}_{3+\delta}$ has recently been speculated [12] to drastically modify the e_g splitting due to a strong reduction of the apical oxygen distance, bringing into play both the $3d_{x^2-y^2}$ and $3d_{3z^2-r^2}$ orbital.

In this Letter, we particularize on the analysis of an effective two-band model spanned by the e_g orbital space of transition metal oxides, and investigate the onset of superconducting order. While variants of this model have already been studied in the context of overdoped cuprate superconductors in general [13] and $\text{Ba}_2\text{CuO}_{3+\delta}$ in particular [14], we create a synoptic perspective on multi-orbital effects by comparing the high- T_c material $\text{Ba}_2\text{CuO}_{3+\delta}$ (BCO) to the low- T_c regime of $\text{LaNiO}_3/\text{LaAlO}_3$ (LNO/LAO) heterostructures. The rare-earth nickelates, with a close similarity between the NiO_2 and CuO_2 planes, have recently surfaced as potentially cuprate related unconventional superconductors [15] and, since the finding of T_c up to 15 K in NdNiO_2 , have established an exciting domain, in which even higher T_c 's may be realized [16]. An earlier idea in this direction [8], followed up by LDA+DMFT electronic structure calculations [9], suggested turning a nickelate Fermi Surface (FS) into a cuprate-like one by orbital engineering via heterostructuring: sandwiching a LaNiO_3 layer between layers of an insulating oxide, such as LaAlO_3 , will confine the $3d_{3z^2-r^2}$ orbital in the z -direction, removing this band from the FS. This way, one restricts the electron to the $3d_{x^2-y^2}$ orbital, similar to the conventional cuprate case. The DMFT calculation of Reference [9] yields a single-sheet FS with a small (30%) $3d_{3z^2-r^2}$ component.

The more recent experimental finding of a T_c of only 3K in related heterostructures, however, challenges the hitherto belief that T_c is optimized when the $3d_{x^2-y^2}$ orbital weight is concentrated in a single band.

Following up on previous work, we compare the high- T_c to the low- T_c regime of the e_g two-orbital Hubbard model by employing a toolkit composed of a variety of numerical methods. Our analysis is performed through Kohn-Luttinger (KL) type calculations [17, 18] in the weak-coupling and through functional renormalization group (FRG) [7, 19] as well as random phase approximation (RPA) [20–22] studies in the intermediate-coupling regime. We find that, most importantly, the e_g energy splitting and the orbital filling turn out to be crucial parameters to unravel different superconducting orders, and drastically varying pairing strengths. All methods yield d -wave and extended s -wave pairing as the leading and subleading superconducting orders in the high- T_c regime. The ordering hierarchy in the low- T_c regime becomes significantly more susceptible to even a small change of parameters, and hence less universal.

e_g minimal model.— The shared geometry of the TO_2 ($T = \text{Ni}, \text{Cu}$) planes leads to similarities of the ratios of different transition matrix elements $t_{o'o,\alpha}$ between neighbouring sites, as established by ab initio density functional theory (DFT) calculations (See Supplemental Material SM) yielding band structures such as Figure 1. This allows us to identify two critical parameters that distinguish the high- T_c material BCO from the low- T_c nickelate heterostructure. The first is the e_g manifold splitting ϵ caused by Jahn-Teller distortions of the oxygen octahedra, which is significantly enhanced in the cuprate system (0.87 eV) compared to the nickelate system (0.11 eV). The second crucial distinction, which is particularly visible through the paradigmatic material limits cuprates and nickelates, is given by the doping level δ . While the transition metal ion in both cases is nominally given by $3d^7$ for LNO/LAO and Ba_2CuO_4 , reducing the oxygen doping in BCO δ will increase the filling of the d -shell up to a $3d^9$ configuration for Ba_2CuO_3 . In our model, this is taken into account by increasing the filling of the e_g subspace for BCO to $n = 2$ electrons. The Hamiltonian we adopt for both materials (albeit with different parameters) is given by

$$H_0 = \sum_{i,\sigma} \sum_{o=1,2} \left((-1)^o \frac{\epsilon}{2} - \mu \right) c_{o,i,\sigma}^\dagger c_{o,i,\sigma} + \sum_{i,\sigma} \sum_{j \neq i} \sum_{o',o=1,2} t_{o'o,\alpha(i,j)} c_{o',i,\sigma}^\dagger c_{o,j,\sigma}, \quad (1)$$

where $c_{o,i}^\dagger$ creates an electron in the orbital $o = 1, 2$ ($d_{x^2-y^2}, d_{3z^2-r^2}$) on site \vec{r}_i . The index $\alpha(i, j)$ counts the proximity of different sites i and j and is used to label the corresponding orbital hybridizations $t_{o'o,\alpha}$, ϵ indicates the size of the onsite energy difference for the relevant orbitals and the chemical potential μ controls the filling

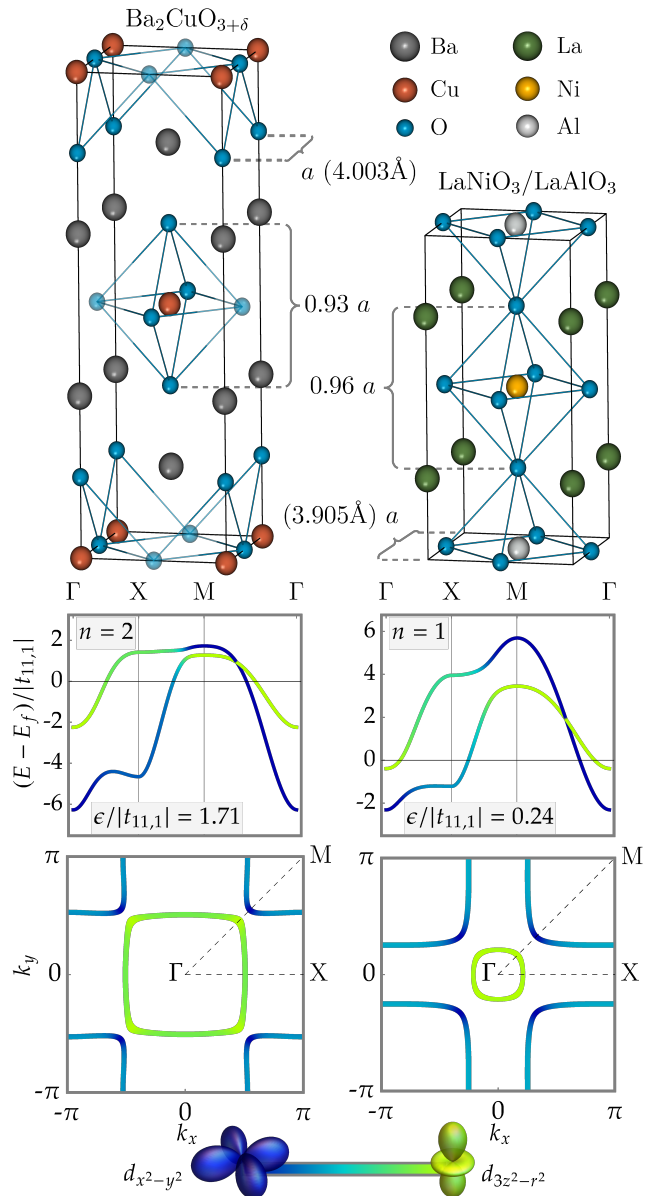


Figure 1. Sketch of unit cell, band structure and Fermi surface for BCO (unit cell for $\delta = 1$, left) and LNO/LAO (right). The orbital weight of a state is given by the respective color blend of blue ($d_{x^2-y^2}$) and green ($d_{3z^2-r^2}$), we indicate the density of states on the Fermi surface by the thickness of the line.

of the system. Starting from DFT-calculations [23, 24] for our prototypical material instances LNO/LAO and BCO, the tight-binding parameters for this low energy model were obtained by projecting the DFT result onto a pair of maximally localized Wannier orbitals on the transition metal ions [25]. The resulting model parameters for both LNO heterostructures and BCO are given in the SM.

Despite the different material chemistry, the similarity of the obtained parameter sets after normalizing to the bandwidth is remarkable, given the strongly differing

T_c . We are able to identify two significant differences: (i) the orbital splitting and (ii) the filling fraction of the e_g doublet. While the orbital splitting mainly controls the energy splitting of the bands at the Γ point as well as the orbital hybridization, the resulting differences in the Fermiology, seen in Figure 1, result primarily from the difference in the chemical potential.

We model the interaction by adopting a Kanamori type interaction Hamiltonian, comprising the four onsite interaction terms in the considered multi-orbital model

$$\begin{aligned}
H_I = & U \sum_{i,o} c_{o,i,\uparrow}^\dagger c_{o,i,\uparrow} c_{o,i,\downarrow}^\dagger c_{o,i,\downarrow} \\
& + V \sum_{i,\sigma,\sigma'} c_{1,i,\sigma}^\dagger c_{1,i,\sigma} c_{2,i,\sigma'}^\dagger c_{2,i,\sigma'} \\
& + J \sum_{i,\sigma,\sigma'} c_{1,i,\sigma}^\dagger c_{2,i,\sigma'}^\dagger c_{1,i,\sigma} c_{2,i,\sigma'} \\
& + J' \sum_{i,o \neq o'} c_{o,i,\uparrow}^\dagger c_{o,i,\downarrow}^\dagger c_{o',i,\downarrow} c_{o',i,\uparrow},
\end{aligned} \tag{2}$$

with intra-orbital (U), inter-orbital (V) repulsive interactions as well as Hunds coupling (J) and pair hopping terms (J'). The orbital makeup of the BCO bands at the Fermi level are cleaner than the ones of LNO/LAO due to the larger orbital splitting ϵ . As a consequence, inter- (intra-) orbital interactions and inter- (intra-) pocket/band interactions correlate more strongly in the case of BCO compared to LNO/LAO.

The interaction parameters for the approximation of a rotationally invariant system are given by $V = U - 2J$ and $J' = J$ [26, 27]. We further fix $J = 0.25 U$ (resulting in $V = U/2$) and are subsequently left with the overall interaction scale U as the only free parameter. Since the rotational symmetry of the e_g complex is broken by the octahedral crystal field, it is interesting to compare interaction schemes beyond this simple modelling. The ratio of inter- versus intra-orbital interaction strength hence is a reasonable parameter to explore, and we further use it to gain additional insight into multi-orbital interaction effects in our effective model. While actual materials will be limited to the vicinity of $V/U \approx 1/2$, it is revealing to fully probe the available parameter space, as implemented in the SM. For the remainder of the main text, we fix $V = U/2$ and choose the overall interaction scale appropriately [18, 28] (see also SM).

Results.—In order to get a first impression of the primary spin fluctuation channels, we analyze the bare particle-hole susceptibility

$$\begin{aligned}
\chi_0(\mathbf{q}, \omega) = & \sum_{oo'} \sum_{\mathbf{k}, i\bar{\omega}_n} \left(G_{\mathbf{k}+\mathbf{q}, \omega+i\bar{\omega}_n}^{oo'} G_{\mathbf{k}, i\bar{\omega}_n}^{o'o} \right) \\
= & \sum_{oo'} \chi^{oo'}(\mathbf{q}, \omega).
\end{aligned} \tag{3}$$

It is determined by the single-particle Green's functions $G_{\mathbf{k}, i\bar{\omega}_n}^{oo'}$ and hence independent of the employed approximations for the treatment of interactions beyond DFT.

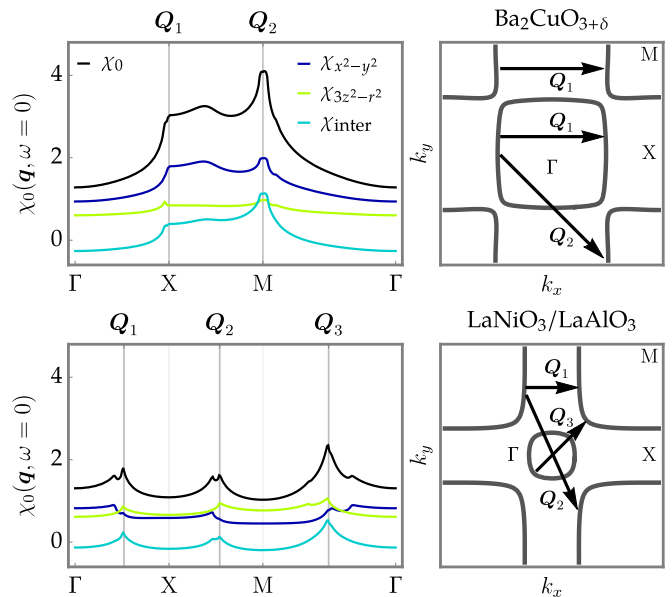


Figure 2. Bare susceptibility in arbitrary units for BCO (top panel) and LNO/LAO (bottom panel) with $\chi^{11} = \chi_{x^2-y^2}$, $\chi^{22} = \chi_{3z^2-r^2}$, and $\chi^{12} + \chi^{21} = \chi_{\text{inter}}$ and leading nesting vectors shown in the corresponding BZ (right hand side).

We show its zero frequency limit in Figure 2 and highlight corresponding nesting features of the Fermi surface. In contrast to LNO/LAO, which shows an overall uniform bare susceptibility, the nesting in BCO is strongly enhanced for the transfer momenta $\mathbf{Q}_1 = (\pi, 0)$, $(0, \pi)$ and $\mathbf{Q}_2 = (\pi, \pi)$. These commensurate nesting vectors induce pronounced spin fluctuations in the system which will finally result in attractive interaction channels for the pair-scattering vertex (see e.g. Reference [3]).

As we analyze the onset of superconductivity for LNO/LAO and BCO in our effective model, this is pursued through different methods: a Kohn-Luttinger type analysis [17, 18], which is asymptotically exact at infinitesimal coupling, is complemented by random phase approximation [20–22] as well as functional renormalization group [7, 19] calculations that are usually employed within the intermediate coupling regime. In the main Letter text, we constrain ourselves mainly to the presentation of the fRG results, and refer the reader to the detailed SM for additional information. Since the material instances are most likely located in the intermediate coupling regime, the fRG provides the most systematic treatment of superconductivity, as it treats all particle-hole and particle-particle channels on equal footing. It thus allows to most directly resolve the connection between spin fluctuations channels and superconductivity. Still, one needs to stay aware of the fact that all numerical methods at intermediate coupling are just approximations. Due to this, we also added the Kohn-Luttinger analysis, in order to have a rigorous reference point at infinitesimal coupling [29].

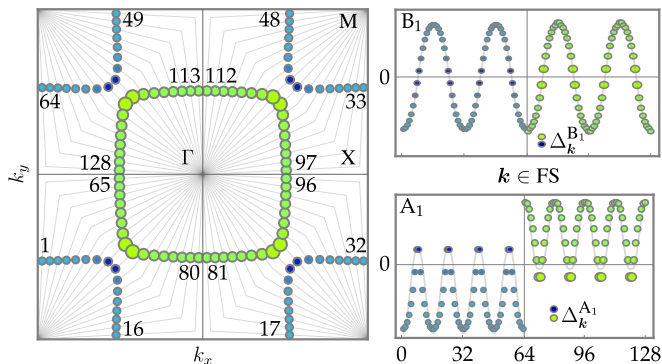


Figure 3. Fermi surface (left) of BCO discretized in patches (1-128) for the numerical fRG study. The color scheme, representing the orbital weights, is in accordance with Figure 1 and the thickness of the plot marker indicates the DOS. On the right hand side we plotted the form factor of the leading (upper panel) and sub leading (lower panel) eigenvalue λ for the superconducting channel on the discretized Fermi surface at the break down of the fRG flow. They transform according to the B_1 and A_1 irreducible representations of the lattices C_{4v} point group symmetry respectively. The fitted harmonic fingerprint of these form factors is indicated by the grey lines in the panels on the right.

Within fRG, we determine the critical cutoff energy Λ_c and effective two particle irreducible vertex $\Gamma^{\Lambda_c}(\mathbf{k}_1, \mathbf{k}_2, \mathbf{k}_3, \mathbf{k}_4)$ for our effective model. As with all other methods used, a short review of the fRG methodology is delegated to the SM. The renormalization flow breaks down at Λ_c *i.e.*, the entries of Γ^{Λ_c} diverge so that we can classify the leading instability by decomposing the full effective vertex Γ^{Λ_c} into mean-field channels. For superconductivity, we obtain the effective Cooper pair interaction $\Gamma^{\text{SC}, \Lambda_c}(\mathbf{k}, \mathbf{k}') = \Gamma^{\Lambda_c}(\mathbf{k}, -\mathbf{k}, \mathbf{k}', -\mathbf{k}')$. By solving the linearized gap equation

$$\lambda \Delta_{\mathbf{k}} = \sum_{\mathbf{k}'} \Gamma^{\text{SC}, \Lambda_c}(\mathbf{k}, \mathbf{k}') \Delta_{\mathbf{k}'} \quad (4)$$

with $\Lambda_c \propto T_c$, we identify the symmetry class of the superconducting gap function $\Delta_{\mathbf{k}}$ for the smallest eigenvalue λ at Λ_c .

Figure 3 displays the gap functions for the leading and subleading eigenvalues λ for BCO. We find a cuprate-like $d_{x^2-y^2}$ -wave form factor for the leading eigenvalue of $\Gamma^{\text{SC}, \Lambda_c}(\mathbf{k}, \mathbf{k}')$ and extended s -wave order for the sub-leading eigenvalue. Assigning the associated irreducible lattice representation (irrep), the leading eigenvalue possesses the symmetry character B_1 with $\Delta_{\mathbf{k}}^{B_1} \propto (\cos k_x - \cos k_y) + 0.001 (\cos 2k_x - \cos 2k_y)$ and the subleading one A_1 with $\Delta_{\mathbf{k}}^{A_1} \propto (\cos k_x + \cos k_y) + 0.45 (\cos 3k_x + \cos 3k_y)$. The harmonic decomposition of these form factors is obtained by fitting to the fRG eigenvectors. For BCO, these results agree with the RPA results presented in the SM [?], which in turn reproduce previous RPA results by Maier *et al.* [14].

Method	$\text{Log}_{10} \left(\frac{T_c^{\text{LNO/LAO}}}{T_c^{\text{BCO}}} \right)$	(sub-)leading irrep	
		BCO	LNO/LAO
fRG	$\mathcal{O}(-2)$	B_1 (A_1)	E (B_2)
RPA	$\mathcal{O}(-10)$	B_1 (A_1)	B_2 (B_1)
KL	$-408(\text{eV}^2)/U^2$	A_1 (B_1)	E (B_2)

Table I. Ratio of the critical temperature for LNO/LAO and BCO calculated by fRG (functional RG), RPA (Random Phase Approximation), and KL (Kohn-Luttinger) analysis and the corresponding classification of the gap function in irreducible lattice representations (irreps). The irreps are often named according to their nodal structure: A_1 is referred to as an (extended) s -wave, E as a p -wave and $B_1(B_2)$ as $d_{x^2-y^2}(d_{xy})$.

It is quite transparent in fRG, how these superconducting orders relate to the pronounced spin fluctuation channels: the B_1 and A_1 form factors are enhanced by the dominant pair scattering process with momentum transfer \mathbf{Q}_2 , and partially by \mathbf{Q}_1 . The corners of the Fermi surface are favourably nested to a majority of the momenta on the same Fermi pocket via \mathbf{Q}_1 and the corners of the other Fermi pocket via \mathbf{Q}_2 , yielding additional nodes and a particularly anisotropic A_1 form factor.

By contrast, the fRG analysis of LNO/LAO yields an upper bound for T_c which is two orders lower in magnitude, and a form factor transforming under the E irrep of the crystal's point group. The Fermi pockets feature no particularly pronounced nesting which, combined with the unclear orbital makeup, yields a nearly uniform pairwise interaction between different points of the Fermi surface. As a consequence, Λ_c is dramatically decreased compared to the BCO results.

We present the symmetry class of the leading form factor and the ratio of T_c for BCO and LNO/LAO in Table I for the fRG, RPA, and KL calculations. A unanimous finding of all methods is the overall trend of lower T_c for LNO/LAO as well as the leading $d_{x^2-y^2}$ - and s -wave instabilities for the high- T_c case in BCO. For LNO/LAO, all methods substantially differ from each other. Given the small instability scale and, from there, the enhanced sensitivity of the result to the specific formulation of the approximative method, this is not surprising. It shows, that in the low- T_c , or rather pairing noise, regime, even slight biases of different approximation schemes manage to affect the eventual result, and strongly enhances the volatility of any result for the superconducting instability. Nevertheless, it is still interesting to trace back the biases of the different methods in such a case, which is delegated to the SM.

Conclusion.—Already in an effective description as simple as the e_g minimal model studied in this work, we can identify the enormous range of multi-orbital effects on T_c at the example of a multi-orbital high- T_c material $\text{Ba}_2\text{CuO}_{3+\delta}$ and a multi-orbital low- T_c material $\text{LaNiO}_3/\text{LaAlO}_3$. Certainly, this study is not exhaustive in describing all multi-orbital effects in transition metal

superconductors. For instance, not only multiple orbitals of the transition metal atom, but also other orbital degrees of freedom may prevail at low energies, such as recently observed for infinite layer nickelates. Still, we expect the minimal modelling of multi-orbital effects to constitute a promising future direction to close the gap between experimental evidence and theoretical simulation of unconventional superconductors.

Acknowledgments.—This work is funded by the Deutsche Forschungsgemeinschaft (DFG, German Research Foundation) through Project-ID 258499086 - SFB 1170 and through the Würzburg-Dresden Cluster of Excellence on Complexity and Topology in Quantum Matter-ct.qmat Project-ID 390858490 - EXC 2147. SR acknowledges support from the Australian Research Council through FT180100211 and DP200101118. We further gratefully acknowledge the Gauss Centre for Supercomputing e.V. [30] for providing computing time on the GCS Supercomputer SuperMUC at Leibniz Supercomputing Centre [31] and the HPC facility Spartan hosted at the University of Melbourne.

Supplemental Material

From high- T_c to low- T_c : Multi-orbital effects in transition metal oxides

FIRST-PRINCIPLES ANALYSIS

We performed first-principles calculations within the framework of the density functional theory (DFT) as implemented in the QUANTUM ESPRESSO suite [23, 24]. The generalized gradient approximation, as parametrized by the Perdew-Burke-Ernzerhof generalized gradient approximation (PBE-GGA) functional for the exchange-correlation potential, was used by expanding the Kohn-Sham wave functions into plane waves up to an energy cutoff of 100 Ry \approx 1.4 keV and sampling the Brillouin zone on a $4 \times 4 \times 2$ regular mesh [32]. For Ba_2CuO_4 we used the crystal structure parameters available from experiment [12] ($a = 4.003 \text{ \AA}$, $c = 12.94 \text{ \AA}$). Due to the absence of experimental data on the $\text{LaAlO}_3/\text{LaNiO}_3$ heterostructure (LAO/LNO) proposed in [8, 9], we simulated its epitaxial growth by imposing an in-plane lattice constant of $a = 3.905 \text{ \AA}$ and relaxing the out of plane lattice parameter as well as the atomic positions on a refined $24 \times 24 \times 24$ regular mesh Brillouin zone mesh, resulting in $c = 7.500 \text{ \AA}$. The extraction of the two-orbital minimal model used in the presented analysis of superconducting instabilities in both materials was based on the Wannier functions formalism [25] and we fixed the Fermi level in our model by enforcing the filling in the simplified model as opposed to the DFT Fermi level.

MINIMAL MODEL

The minimal model to describe the low energy physics of both materials studied here is an extended two-band Hubbard model on a square lattice. While this becomes apparent from the performed DFT calculations, one can also arrive at this conclusion by simple chemistry considerations: Both the LAO/LNO and $\text{Ba}_2\text{CuO}_{3+\delta}$ feature a layered perovskite structure. In case of LNO/LAO nickel oxide planes $\text{Ni}^{3+}\text{O}_2^{2-}$ alternate with an insulating aluminium oxide plane $\text{Al}^{3+}\text{O}_2^{2-}$, allowing for a two-dimensional description of the low energy electronic degrees of freedom located on the nickel ions [9]. For BCO, copper oxide planes $\text{Cu}^{(2+2\delta)+}\text{O}_2^{2-}$, which are pairwise shifted against each other, alternate with two insulating barium oxide planes $\text{Ba}_2^{2+}\text{O}_2^{2-}$. As such, both systems yield a two-dimensional description of the low energy electronic degrees of freedom located on the copper or nickel ions [12, 14].

As it is typical for perovskite structures, the transition metal ion is enclosed by an octahedron of O^{2-} ions. This results in a crystal field which splits the $L = 2$ d-orbital quintuplet into a low energy t_{2g} triplet (composed of the

d_{xy} , d_{xz} and d_{yz} orbitals) and an e_g doublet (composed of the remaining $d_{x^2-y^2}$ and $d_{3z^2-r^2}$) with higher energy. For both LNO/LAO ($\text{La}^{3+}\text{Ni}^{3+}\text{O}_3^{6-}/\text{La}^{3+}\text{Al}^{3+}\text{O}_3^{6-}$) and Ba_2CuO_4 ($\text{Ba}_2^{4+}\text{Cu}^{4+}\text{O}_4^{8-}$) the transition metal ions nickel and copper have a $3d^7$ electronic configuration, while the $3d^6$ configuration on the aluminum site of LNO/LAO results in a significant excitation gap allowing us to remove it from the low energy description of the system. In the case of BCO, we additionally simulate the oxygen deficiencies by artificially raising the Fermi level in our model compared to the Ba_2CuO_4 calculation, simulating the effect of the added electrons by removing oxygen from the compound.

The completely filled t_{2g} multiplet is split of by the octahedral crystal field, allowing us to restrict our analysis to the e_g doublet. Additionally, degeneracy of the e_g states is lifted by distortions of the oxygen octahedron. The strength of this Jahn-Teller distortion and the resulting e_g splitting ϵ is one of the key parameters resolved in our work. We find our effective low-energy model to be formed by a two band Hubbard model on a square lattice spanned by the transition metal's $d_{x^2-y^2}$ ($o = 1$) and $d_{3z^2-r^2}$ ($o = 2$) orbitals:

$$H_0 = \sum_i \sum_{o=1}^2 \left((-1)^o \frac{\epsilon}{2} - \mu \right) c_{o,i}^\dagger c_{o,i} \quad (5)$$

$$+ \sum_i \sum_{j \neq i} \sum_{o',o=1}^2 t_{o'o,\alpha(i,j)} c_{o',i}^\dagger c_{o,j} \quad (6)$$

$$= \sum_i \sum_k \sum_{o',o=1}^2 \xi_{o'o}(\vec{k}) c_{o',k}^\dagger c_{o,k}$$

with the single-particle bands

$$\xi_{oo}(\vec{k}) = \left((-1)^o \frac{\epsilon}{2} - \mu \right) + 2t_{oo,1}(\cos k_x + \cos k_y) \\ + 4t_{oo,2} \cos k_x \cos k_y + 2t_{oo,3}(\cos 2k_x + \cos 2k_y),$$

$$\xi_{oo'}^{o \neq o'}(\vec{k}) = 2t_{oo',1}(\cos k_x - \cos k_y) \\ + 2t_{oo',3}(\cos 2k_x - \cos 2k_y),$$

where $c_{o,i}^\dagger$ creates an electron in the orbital $o = 1, 2$ ($d_{x^2-y^2}$, $d_{3z^2-r^2}$) on site \vec{r}_i . The index $\alpha(i, j)$ counts the proximity of different sites i and j and is used to label the corresponding orbital hybridizations $t_{oo,\alpha}$. The chemical potential μ controls the filling of the system and ϵ is the relative onsite energy of the relevant orbitals. Tab. II lists the tight binding parameters for the minimal model that we obtained by fitting this model to the results from our DFT calculations.

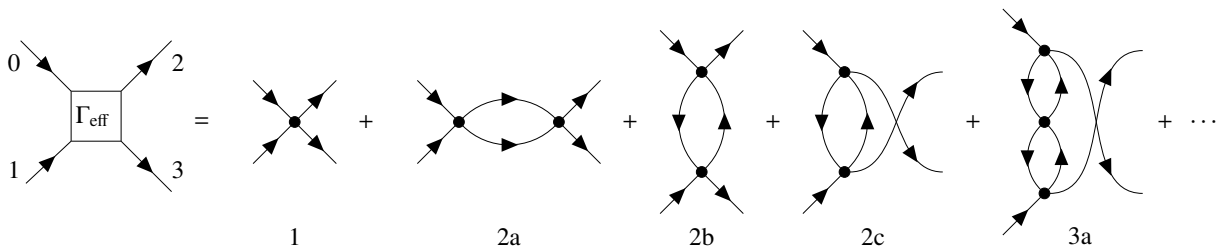


Figure 4. Diagrammatic expansion of the effective two-particle-vertex Γ_{eff} in perturbation theory. Internal lines represent fermionic propagators and solid points represent the bare two particle interaction Γ_b . There are three topological different diagrams up two second order in Γ_b . We absorb all additional factors and signs in their respective diagram. Depending on the method different diagrams are chosen as explained in the corresponding subsections.

model parameters	Ba ₂ CuO _{3+δ}	LaNiO ₃ /LaAlO ₃
t_0 / eV	-0.511	-0.447
$n / \text{electrons}$	2.00	1.00
$\epsilon / t_0 $	1.71	0.24
$\mu / t_0 $	0.82	-1.81
hopping amplitudes $/ t_0 $		
$t_{11, \alpha=1}$	-1.00	-1.00
$t_{22, \alpha=1}$	-0.44	-0.48
$t_{12, \alpha=1}$	0.63	0.62
$t_{11, \alpha=2}$	0.13	0.13
$t_{22, \alpha=2}$	-0.07	-0.07
$t_{12, \alpha=2}$	0.00	0.00
$t_{11, \alpha=3}$	-0.28	-0.13
$t_{22, \alpha=3}$	-0.06	-0.03
$t_{12, \alpha=3}$	0.11	0.06

Table II. Parameters for the tight binding Hamiltonian (5) for both LNO/LAO and BCO. $t_{oo', \alpha}$ denotes the hybridization between two orbitals o and o' that are α^{th} nearest neighbours ($\alpha = 1$ corresponds to nearest neighbour, $\alpha = 2$ to next-nearest neighbour etc.).

METHODOLOGY

In this section we aim to give a short overview on different diagrammatic schemes to calculate the effective two-particle vertex function, the central object to reveal the superconducting instabilities. Specifically, we perform Kohn-Luttinger type calculations [17, 18] in the weak coupling (referred to as weak-coupling renormalization group Kohn-Luttinger analysis (KL) in the following) and through functional renormalization group (FRG) [7, 19] as well as random phase approximation (RPA) [33] in the intermediate coupling regime. Fig. 4 shows the perturbative expansion of the effective two-particle vertex Γ_{eff} in terms of the bare two-particle vertex Γ_b . We will show how one can use these diagrams to calculate Γ_{eff} within KL analysis and RPA. Further we give a short derivation of the fRG method, which features the same topological diagrams as the KL analysis, in order to solve

a differential equation to determine Γ^{Λ_c} , where Λ_c is the critical energy scale of the system. Clearly all methods employed here include different sets of diagrams, resulting in a significant difference of captured screening effects. Therefore it is necessary to tailor the initial interaction strength U for each approximation scheme individually, in order to obtain comparable results. A more detailed Discussion is presented in the References [18, 28]. Here we choose $U = 3.5 \text{ eV}$ for the fRG calculations and $U = 0.8 \text{ eV}$ for the RPA calculation and therefore account for the additional screening processes include in the fRG approximation.

Functional Renormalization Group

Method.—The here presented summary of the FRG method follows Ref. 7, which provides a detailed derivation of the flow equation. First we set up our theory at a high energy scale Λ_{init} with the action

$$S^{\Lambda_{\text{init}}} = S_0 + S_I,$$

containing the bare action S_0 and an interaction term S_I . In order to connect to lower energy scales we integrate out high-energy modes step by step, adjusting the action accordingly and generating a trajectory between microscopic theory at high energies and an effective low-energy description. We achieve this by introducing a flow parameter Λ interpolating the action from the trivial starting point ($\Lambda = \Lambda_{\text{init}}$) to the fully interacting theory ($\Lambda = 0$). One can deduce a set of integro-differential equation for all irreducible $2n$ -point vertex functions. It turns out that the hierarchy of these so called flow equations does not close, meaning that in order to calculate the flow for an $2n$ -point vertex function, one has to know the vertex function of the next higher order. Consequentially, to numerically solve the integro-differential equation, the flow equation for the four-point vertex function is truncated by neglecting all terms containing higher order vertex functions [19, 34]. Also we neglect any corrections of the self energy Σ under the flow. The remaining integro-differential equation is of first order. The derivative of the irreducible four-point

vertex function $\Gamma_{k'_1, k'_2; k_1, k_2}^{(4), \Lambda}$ with respect to Λ turns out to be equal to diagrams which are topologically equivalent to $2a - 2c$ in Fig. 4, the only difference being that one

$$\frac{d}{d\Lambda} \Gamma_{k'_1, k'_2; k_1, k_2}^{(4), \Lambda} = \sum_{\substack{k, k' \\ q, q'}} G_{k, k'}^\Lambda S_{q, q'}^\Lambda \left(\Gamma_{k'_1, k'_2; k, q}^{(4), \Lambda} \Gamma_{k', q'; k_1, k_2}^{(4), \Lambda} - \left[\Gamma_{k'_1, q'; k_1, k}^{(4), \Lambda} \Gamma_{k', k'_2; kq, k_2}^{(4), \Lambda} + (k \leftrightarrow q, k' \leftrightarrow q') \right] \right. \\ \left. + \left[\Gamma_{k'_2, q'; k_1, k'}^{(4), \Lambda} \Gamma_{k', k'_1; q, k_2}^{(4), \Lambda} + (k \leftrightarrow q, k' \leftrightarrow q') \right] \right).$$

An index k contains the spin σ , orbital (band) o (b), momentum \mathbf{k} and frequency k_0 degrees of freedom; the k index on the left corresponds to an in-going particle, while the one on the right to an out-going particle. We further simplify the numerical effort by projecting all momenta to the Fermi surface and compute the flow neglecting all finite frequency contributions.

There are multiple schemes to implement the flow parameter. Wilson's original idea of integrating out momentum modes shell by shell offers one possible implementation [35–37], by introducing an energy cutoff depending on Λ in the propagators. However this cutoff scheme is not suited to treat particle-hole fluctuations in an unbiased way [7]. Alternatively, temperature can be used as the flow parameter, as utilized in this work. Doing so not only avoids any issues with the particle hole fluctuations but also offers a very intuitive picture of understanding the flow as a whole. Integrating out energy modes, descending from high to low energies, can now be interpreted as cooling down our system.

Using the Euler method, we can solve the integro-differential equation. The initial value for the action is chosen to be equivalent to the bare action

$$S^{\Lambda_{\text{init}}} = S_0 \quad (7)$$

and the initial four-point vertex function at Λ_{init} is set to be the interaction term of the unrenormalized theory, which then flows under the set up formalism either to a new effective function at $\Lambda = 0$ or to a fix point at a given Λ_c at which the vertex diverges and the flow breaks down. The later case marks the breakdown of the Fermi surface to a new symmetry broken phase. The order parameter of the new phase can be analyzed by decomposing the full vertex function into mean field channels. The leading instability is then given by the most diverging of these channels. Analogously to RPA and KL analysis one can further characterize the order parameter according to its transformation behavior under the lattices symmetries, as demonstrated in the main paper.

Results.—Fig. 5 shows the critical cutoff energy Λ_c for the two relevant models. The superconducting channel of the meanfield decoupled effective vertex $\Gamma^{Sc, \Lambda_c}(k, k')$

of the internal Green's functions G^Λ gets promoted to a single scale propagator $S^\Lambda = \partial_\Lambda G^\Lambda|_{\Sigma=\text{const}}$.

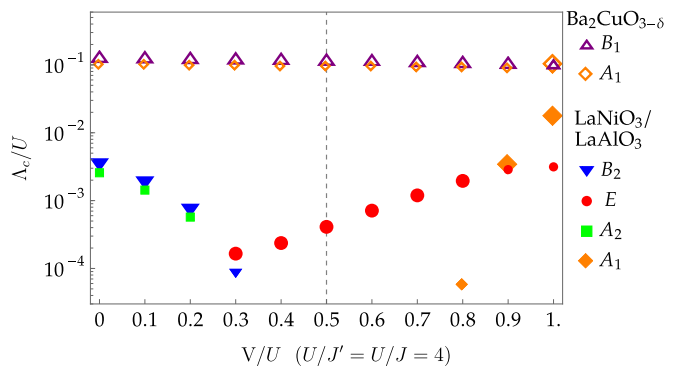


Figure 5. Critical cutoff Λ_c of fRG-flow and symmetry character of leading and subleading superconducting order parameter for for BCO (unfilled markers) and LNO/LAO (solid markers). The cutoff for the subleading order parameter is estimated by extrapolating the divergence in Λ beyond Λ_c of the corresponding eigenvalue λ . The interaction is given by $U = 4J = 4J' = 3.5$ eV while the different values for V/U is achieved by increasing V . The dashed line indicates the generic interaction ratio $U = 2V = 4J = 4J'$.

at Λ_c can further be analysed by solving the eigenvalue equation

$$\Delta_k \lambda = \sum_{k'} \Gamma^{Sc, \Lambda_c}(k, k') \Delta_{k'} \quad \text{with} \quad \Lambda_c \propto T_c \quad (8)$$

and identifying the symmetry class of the form factor Δ_k for the smallest eigenvalue λ .

By doing so we can identify two regimes: The first being the case of $V \geq U$, a regime featuring strong repulsive interaction between the pockets of the Fermi surface (FS), which are dominated by opposite orbital character, resulting in an extended s -wave (A_1 irrep), featuring nodes between the pockets. The other being $V \ll U$, where intra-pocket scattering makes up for nearly all scattering processes and thus features nodal lines intersecting the FS. In case of $\text{Ba}_2\text{CuO}_{3+\delta}$ the leading symmetry class is given by B_1 irrep ($d_{x^2-y^2}$ -wave), which is the well known $d_{x^2-y^2}$ -wave present in most cuprates, to accommodate the large intra orbital nesting $q = (\pi, \pi)$. For $\text{LaNiO}_3/\text{LaAlO}_3$ the nature of the incommensurate nest-

ing vectors would favour nodes between the parallel lines of the outer and inner pocket of the Brillouin zone (BZ). The resulting nodal configuration can be accommodated by a form factor of the symmetry class B_2 (d_{xy} -wave) and the subleading form factor of the symmetry class A_2 (g -wave).

In between these two regimes the critical cutoff for $\text{Ba}_2\text{CuO}_{3+\delta}$ is nearly constant. By increasing the inter orbital interaction nesting between the parallel lines of the FS of different pockets, connected by transition vectors around $\mathbf{q} = (\pi, \pi)$, become relevant, hence the symmetry remains B_1 . Note that the nesting vectors around $\mathbf{q} = (\pi, \pi)$ are yielding favourable results in the gap equation for the B_1 and A_1 order parameters. Hence, the transition between these two phases by increasing inter-orbital interactions is quite generic: one just chooses between the nodal configuration which achieves a sign change between the maximal subset of nesting vectors weighted with their interaction strength. This can also be seen in the weak coupling analysis below and in the RPA results from Maier *et al.* [14], where the eigenvalues associated with B_1 and A_1 irreps are nearly degenerate. In fRG these two irreps make up the leading and first subleading symmetry classification of the order parameter for all probed values of V/U with a flow that indicates nearly simultaneous divergences of the respective eigenvalues.

In contrast, for $\text{LaNiO}_3/\text{LaAlO}_3$ there is no such sequence of phases sharing advantageous nesting options at the vicinity of the phase transition. Its intermediate interaction regime offers no clear favoured nesting option and its unclear orbital makeup yields a uniform interaction between different points of the FS. Hence, it features a dramatically decreased Λ_c and a form factor of the symmetry class E (p -wave). This decrease is remarkable for two reasons. Firstly, it is counter intuitive in the sense that we add interaction to the system and decrease T_c by up to two orders of magnitude. Secondly, the resulting form factor of symmetry class E has two representations (*i.e.*, the irrep is two-dimensional), which can be added in such a way that the resulting order parameter leads to a hard gap. The B_2 d -wave is demoted to subleading irrep in this regime, due to the large additional interaction between the two Fermi pockets, which is not aligned with a nodal configuration provided by a d_{xy} order parameter. For $V \approx 0.7 U$ the s -wave becomes the first subleading irrep. Overall it seems very reminiscent to frustration effects in magnetism, although this is not related to the geometry of the system, but instead to the relative mixture of different interactions. Following that line of reasoning one can think of $\text{LaNiO}_3/\text{LaAlO}_3$ as a *frustrated superconductor*.

Electronic structure calculations performed in Ref. [9],

suggested a larger inner FS pocket compared to our results. Increasing the filling of the presented minimal model we find a similar FS (compare Figure 6). The critical cutoffs fRG Λ_c of both fillings are of the same order of magnitude and yield a form factor of symmetry class E , thereby

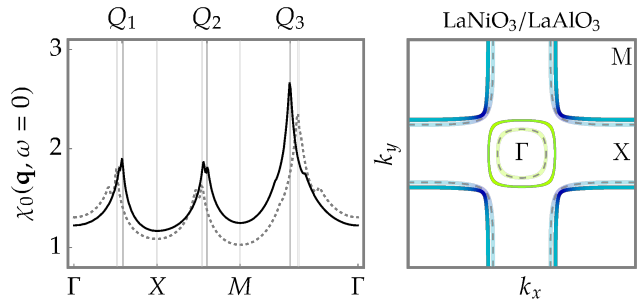


Figure 6. Bare susceptibility and corresponding FS for $\text{LaNiO}_3/\text{LaAlO}_3$ at filling $n = 1.1$ (solid lines) and $n = 1.0$ (dashed line). The respective critical cutoffs for the generic interaction ratio $U = 2V = 4J = 4J'$ and $U = 3.5\text{eV}$ are given by $\Lambda_c/U = 7.1 \cdot 10^{-3}$ ($n = 1.1$) and $\Lambda_c/U = 4.2 \cdot 10^{-3}$ ($n = 1.0$).

demonstrating the independence of the presented many body results from this band structure detail.

Random Phase Approximation

Method.—The RPA formulation is based on the idea that selected particle-hole scattering events add up coherently, whereas all other possible scattering channels are suppressed by acquiring random relative phases. Neglecting these terms in the calculation of the effective two-particle vertex results in a summation up to infinite order of pure bubble and ladder diagrams. For the single orbital case both interactions and susceptibilities are scalar. In contrast the multiorbital case the pairing vertex has an additional contraction over the orbital degrees of freedom. This orbital makeup induces additional diagrams with the structure of vertex corrections which are included in the matrix-RPA formulation [33]. A graphic representation of the considered terms are the particle-hole diagrams shown in Fig. 4 (1, 2b, 2c, 3a, ...).

Firstly we define the bare susceptibility as

$$\chi_{o_1 o_2 o_3 o_4}^0(\mathbf{q}, \tau) = \frac{1}{N} \sum_{\mathbf{k} \mathbf{k}'} \langle T_\tau c_{l_3, \mathbf{k} + \mathbf{q}, \sigma}^\dagger(\tau) c_{l_4, \mathbf{k}, \sigma}(\tau) \times c_{l_2, \mathbf{k}' - \mathbf{q}, \sigma}^\dagger(0) c_{l_1, \mathbf{k}', \sigma}(0) \rangle_0,$$

where o_i are the orbital indices. The bare susceptibility in momentum-frequency space is

$$\chi_{o_1 o_2 o_3 o_4}^0(\mathbf{q}, i\omega_n) = -\frac{1}{N} \sum_{\mu\nu} \sum_{\mathbf{k}} a_{\mu}^{o_4}(\mathbf{k}) a_{\mu}^{o_2*}(\mathbf{k}) a_{\nu}^{o_1}(\mathbf{k} + \mathbf{q}) a_{\nu}^{o_3*}(\mathbf{k} + \mathbf{q}) \frac{n_F(E_{\mu}(\mathbf{k})) - n_F(E_{\nu}(\mathbf{k} + \mathbf{q}))}{i\omega_n + E_{\mu}(\mathbf{k}) - E_{\nu}(\mathbf{k} + \mathbf{q})}.$$

where μ/ν is the band index. $n_F(\epsilon)$ is the Fermi distribution function, $a_{\mu}^{o_i}(\mathbf{k})$ is the o_i -th component of the eigenvector for band μ resulting from the diagonalization of the single-particle Hamiltonian H_0 , and $E_{\mu}(\mathbf{k})$ is the eigenvalue of band μ . The intrinsic spin fluctuations are characterized by the susceptibility. The interacting spin susceptibility and charge susceptibility in RPA level are given by,

$$\chi_1^{RPA}(\mathbf{q}) = [1 - \chi_0(\mathbf{q})U^s]^{-1} \chi_0(\mathbf{q}),$$

$$\chi_0^{RPA}(\mathbf{q}) = [1 + \chi_0(\mathbf{q})U^c]^{-1} \chi_0(\mathbf{q}).$$

Here U^s, U^c are the interaction matrices, which are given by

$$\bar{U}_{o_1 o_2 o_3 o_4}^s = \begin{cases} U & o_1 = o_2 = o_3 = o_4, \\ V & o_1 = o_3 \neq o_2 = o_4, \\ J & o_1 = o_2 \neq o_3 = o_4, \\ J' & o_1 = o_4 \neq o_2 = o_3, \end{cases}$$

$$\bar{U}_{o_1 o_2 o_3 o_4}^c = \begin{cases} U & o_1 = o_2 = o_3 = o_4, \\ -V + 2J & o_1 = o_3 \neq o_2 = o_4, \\ 2V - J & o_1 = o_2 \neq o_3 = o_4, \\ J' & o_1 = o_4 \neq o_2 = o_3, \end{cases}$$

where we used the notation for the Kanamori interaction parameters introduced in the main text.

The effective interaction obtained in the RPA approximation is given by

$$V_{\text{eff}} = \sum_{ij, \mathbf{k}\mathbf{k}'} \Gamma_{ij}(\mathbf{k}, \mathbf{k}') c_{i\mathbf{k}\uparrow}^{\dagger} c_{i-\mathbf{k}\downarrow}^{\dagger} c_{j-\mathbf{k}'\downarrow} c_{j\mathbf{k}'\uparrow}$$

where the momenta \mathbf{k} and \mathbf{k}' are restricted to different FS C_i with $\mathbf{k} \in C_i$ and $\mathbf{k}' \in C_j$, and $\Gamma_{ij}(\mathbf{k}, \mathbf{k}')$ is the pairing scattering vertex. The pairing vertex can be obtained by projecting the pairing vertex in orbital space onto Fermi surfaces,

$$\Gamma_{ij}(\mathbf{k}, \mathbf{k}') = \sum_{\substack{o_1, o_2 \\ o_3, o_4}} a_{v_i}^{o_2*}(\mathbf{k}) a_{v_i}^{o_3*}(-\mathbf{k}) \times \\ \text{Re}[\Gamma_{o_1 o_2 o_3 o_4}(\mathbf{k}, \mathbf{k}', \omega = 0)] a_{v_j}^{o_1}(\mathbf{k}') a_{v_j}^{o_4}(-\mathbf{k}').$$

The orbital vertex function $\Gamma_{o_1 o_2 o_3 o_4}$ for the singlet channel and triplet channel in the fluctuation exchange formulation[38–41] are given by

$$\Gamma_{o_1 o_2 o_3 o_4}^S(\mathbf{k}, \mathbf{k}', \omega) = [\frac{3}{2} \bar{U}^s \chi_1^{RPA}(\mathbf{k} - \mathbf{k}', \omega) \bar{U}^s + \frac{1}{2} \bar{U}^s - \frac{1}{2} \bar{U}^c \chi_0^{RPA}(\mathbf{k} - \mathbf{k}', \omega) \bar{U}^c + \frac{1}{2} \bar{U}^c]_{o_1 o_2 o_3 o_4},$$

$$\Gamma_{o_1 o_2 o_3 o_4}^T(\mathbf{k}, \mathbf{k}', \omega) = [-\frac{1}{2} \bar{U}^s \chi_1^{RPA}(\mathbf{k} - \mathbf{k}', \omega) \bar{U}^s + \frac{1}{2} \bar{U}^s - \frac{1}{2} \bar{U}^c \chi_0^{RPA}(\mathbf{k} - \mathbf{k}', \omega) \bar{U}^c + \frac{1}{2} \bar{U}^c]_{o_1 o_2 o_3 o_4},$$

where $\bar{U}^{s/c} = U^{s/c}(\mathbf{k} - \mathbf{k}')$. χ_0^{RPA} describes the charge fluctuation contribution and χ_1^{RPA} the spin fluctuation contribution. For a given gap function $g(\mathbf{k})$, the pairing strength functional is

$$\lambda[g(\mathbf{k})] = -\frac{\sum_{ij} \oint_{C_i} \frac{dk_{\parallel}}{v_F(\mathbf{k})} \oint_{C_j} \frac{dk'_{\parallel}}{v_F(\mathbf{k}')} g(\mathbf{k}) \Gamma_{ij}(\mathbf{k}, \mathbf{k}') g(\mathbf{k}')}{4\pi^2 \sum_i \oint_{C_i} \frac{dk_{\parallel}}{v_F(\mathbf{k})} [g(\mathbf{k})]^2},$$

where $v_F(\mathbf{k}) = |\nabla_{\mathbf{k}} E_i(\mathbf{k})|$ is the Fermi velocity on a given Fermi surface sheet C_i . From the stationary condition we

find the following eigenvalue problem:

$$-\sum_j \oint_{C_j} \frac{dk'_{\parallel}}{4\pi^2 v_F(\mathbf{k}')} \Gamma_{ij}(\mathbf{k}, \mathbf{k}') g_{\alpha}(\mathbf{k}') = \lambda_{\alpha} g_{\alpha}(\mathbf{k}),$$

where the interaction Γ_{ij} is the symmetric (antisymmetric) part of the full interaction in the singlet (triplet) channel. The leading eigenfunction $g_{\alpha}(\mathbf{k})$ and eigenvalue λ_{α} are obtained from the above equation. The obtained gap function should have the symmetry of one of the irreducible representations for the corresponding point group.

Results.—We show the leading and first subleading eigenvalues calculated within the RPA-matrix formalism

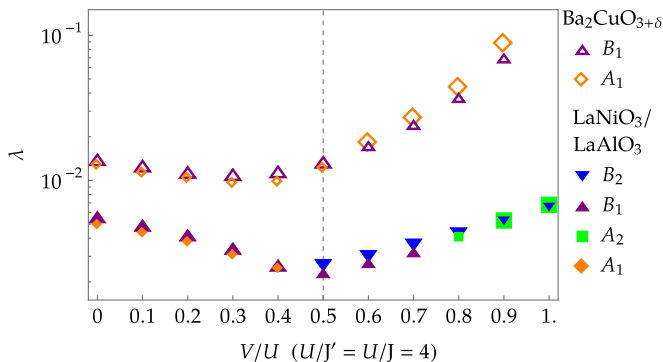


Figure 7. Leading and subleading eigenvalues λ within RPA and symmetry character of the superconducting order parameter of the effective four point RPA vertex Γ for LNO/LAO (solid markers) and for BCO (unfilled markers). The interaction is given by $U = 4J = 4J' = 0.8$ eV and increasing V and $T = 0.02$ eV. The dashed line indicates the the generic interaction ratio $U = 2V = 4J = 4J'$. For BCO Γ diverges for $V/U = 1$, signalling the onset of a spin density wave.

for LaNiO_3 and $\text{Ba}_2\text{CuO}_{3+\delta}$ in Fig. 7. The eigenvalues of $\text{Ba}_2\text{CuO}_{3+\delta}$ are for the whole parameter regime much larger than LaNiO_3 , due to the overall better nesting. As expected, a large regime of interactions is favoring d -wave pairing (B_1 irrep), given the large signal in the bare susceptibility. For $V/U > 1$ the extended s -wave pairing (A_1 irrep), featuring nodes between the Fermi pockets, becomes leading.

In case of LaNiO_3 , there is no clear peak in the bare susceptibility, further the inner Fermi pocket around the Γ -point is largely inert to superconductivity in a repulsive interaction environment, since it features no density fluctuations, is clean in orbital weight, and is in itself not nested. Due to the density distribution of the outer Fermi sheet around the M point, which is enlarged at the edges of the BZ, the resulting B_1 symmetry character is reminiscent of the one band cuprate models. Increasing inter-orbital interactions enlarges the coupling between the parallel lines on the outer Fermi pocket. Hence, additional nodal lines are required, resulting in a B_2 or A_2 symmetry character. Note that there is, similarly to the results of fRG, a pronounced dip in the eigenvalues of LNO/LAO starting at the pure intra-orbital case and increasing inter-orbital interactions.

Using the eigenvalues from the RPA calculations, we can estimate the transition temperature as $T_c \approx \hbar\omega_S e^{-1/|\lambda_{\min}|}$, where $\hbar\omega_S$ is the typical energy scale for spin fluctuations in systems. The T_c of BCO is about 70 K in experiments. To reproduce the experimental value approximately, we take $U = 1$ eV, $J/U = 0.25$, $\hbar\omega_S = 100$ meV and the temperature parameter $T = 0.03$ eV in the Fermi distribution function and then get the dominant pairing state with $\lambda_{\min} = -0.448$ for BCO, leading to the T_c of the order of 100 K. With the same parameters in LNO/LAO, the dominant pairing eigenvalue is 0.005,

much smaller than the case of BCO.

Weak coupling Renormalization Group - Kohn-Luttinger method

Method.—Here, we give a short description of the (KL) method; a detailed discussion can be found in various works [18, 42–46]. Note that one of the most important characteristics of the method is that it becomes asymptotically exact in the limit of infinitesimal coupling, $U \rightarrow 0$.

For the KL analysis, we consider all terms in the perturbative expansion of the effective two-particle-vertex up to second order in the interaction, U , which is given by the first four diagrams in Fig. 4, *i.e.*, diagrams 1, 2a, 2b, and 2c. In contrast to fRG, where higher order diagrams are considered gradually during the flow of the effective interaction parameters, we cut off all diagrams that are of higher than second order in U . In RPA, on the contrary, we sum over a geometric series of only ladder and bubble diagrams, *i.e.*, up to infinite order in U .

The RG flow equation is given by [18, 45, 47]

$$\frac{\partial \Gamma(k_2, k_1)}{\partial \ln(\Omega_0/\Omega)} = - \int_{\text{FS}} dk_3 \Gamma(k_2, k_3) \Gamma(k_3, k_1), \quad (9)$$

where Γ denotes the effective two-particle-vertex, and k_1 and k_2 denote the momenta of the incoming and outgoing pairs of electrons with zero total momentum, respectively. The right hand side is integrated over all Fermi surfaces and we used the short notation $k_i = (n_i, \vec{k}_i)$ with the band index n_i . Ω_0 denotes the initial infrared cutoff and Ω a lowered cutoff. The initial cutoff is chosen in the range

$$U^2/W \gg \Omega_0 \gg W e^{-1/\rho|U|}, \quad (10)$$

where W is the bandwidth. The lower bound ensures that the bare interactions are renormalized due to many-body effects, whereas the upper bound limits all involved modes in the effective interaction to a narrow window around the Fermi surface [18].

In the weak coupling limit we can bypass the procedure of the RG flow, *i.e.*, lowering the cutoff Ω in consecutive steps, and obtain the final Γ directly, where Eq. (10) ensures that the final result does not depend on the initial cutoff, Ω_0 [18]. All terms which contribute in this

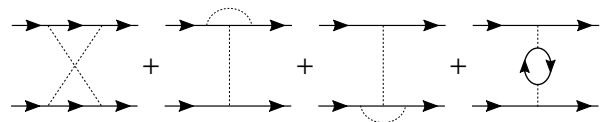


Figure 8. Spinless particle-hole diagrams of the weak coupling expansion of the effective two-particle-vertex in second order in the interaction U . Solid lines represent free particle propagators and dashed lines interactions U .

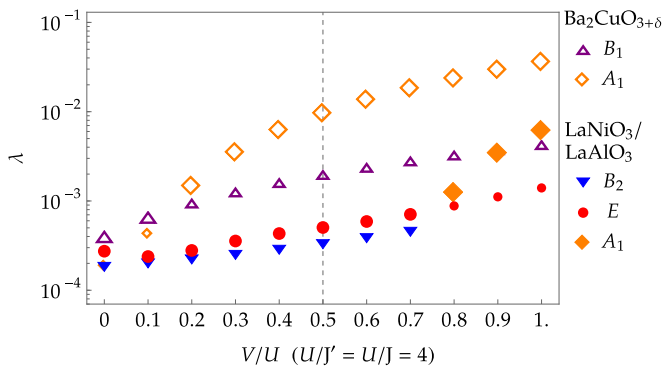


Figure 9. KL Results: leading and subleading Eigenvalues λ and symmetry character of leading superconducting order of effective four point vertex Γ for LNO/LAO (solid markers) and BCO (unfilled markers). The interaction is given by $U = 4J = 4J'$ and increasing V . The dashed line indicates the the generic interaction ratio $U = 2V = 4J = 4J'$.

manner are the diagrams 2b and 2c in Fig. 4, where we use their spinless variants which are given by the four diagrams shown in Fig. 8 (the first order in U diagram just suppresses the plain s -wave solution and can thus be neglected).

In Eq. (9) Γ is scaled such that its eigenvalues λ_i , independently, fulfil

$$\frac{\partial \lambda_i}{\partial \ln(\Omega_0/\Omega)} = -\lambda_i^2. \quad (11)$$

Hence, finding the leading superconducting instability simplifies to an eigenvalue problem for Γ . The effective interaction, $V_{\text{eff}} = \lambda_{\text{min}}/\rho$, of the leading superconducting instability is then obtained from the most negative eigenvalue, λ_{min} (ρ is the total density of states at the Fermi level), and the relation to the critical temperature is given by

$$T_c \sim e^{-1/\rho|V_{\text{eff}}|} = e^{-1/|\lambda_{\text{min}}|}.$$

The corresponding eigenfunction, ψ_{min} , yields the form-factor of the order parameter, which can be classified by the irreducible representations of the symmetry group of the crystal lattice (analogous to the fRG as shown in the main paper).

Results.—The eigenvalues of the leading superconducting instabilities for each irreducible representation obtained from the KL formalism are shown in Fig. 9. Here we plot the eigenvalue λ_{min} as a function of the inter-orbital interaction, V , while keeping the other interactions at $U = 4J = 4J'$.

Firstly, we note that $|\lambda_{\text{min}}|$ for $\text{Ba}_2\text{CuO}_{3+\delta}$ is larger than for LaNiO_3 over the whole parameter range. For both systems, an extended s -wave solution (A_1 irrep) becomes dominant when V/U approaches 1, in agreement with the fRG and RPA results.

For $\text{Ba}_2\text{CuO}_{3+\delta}$, this s -wave (A_1 irrep) is also the leading instability for an extended range around $U = 2V$. For

small V , there is a transition to a $d_{x^2-y^2}$ -wave state (B_1 irrep).

Note that for fRG, for which we used the highest bare interaction the regime of the A_1 irrep in the V/U phase diagram is the smallest compared to the other methods (transition at $V/U \gtrsim 0.9$). In RPA this regime is enlarged (transition at $V/U \approx 0.5 \dots 0.6$) and the KL analysis, where U is infinitesimal yields the largest domain with a leading s -wave (transition at $V/U \approx 0.2 \dots 0.3$)

For LaNiO_3 we find a p -wave (E irrep) solution for most of the shown parameter range, until the transition towards extended s -wave at large values for V .

As mentioned in the main paper, due to the asymptotic character, *i.e.*, the vanishing interacting strength, the KL analysis is extremely sensitive to FS fluctuations; thus differences for the Nickelates compared to RPA and fRG are expected.

* These two authors contributed equally

† stephan.rachel@unimelb.edu.au

‡ rthomale@physik.uni-wuerzburg.de

- [1] J. G. Bednorz and K. A. Müller, Z. Phys. B: Condens. Matter **64**, 189 (1986).
- [2] B. Keimer, S. A. Kivelson, M. R. Norman, S. Uchida, and J. Zaanen, Nature **518**, 179 (2015).
- [3] D. J. Scalapino, Rev. Mod. Phys. **84**, 1383 (2012).
- [4] E. Pavarini, I. Dasgupta, T. Saha-Dasgupta, O. Jepsen, and O. K. Andersen, Phys. Rev. Lett. **87**, 047003 (2001).
- [5] H. Sakakibara, H. Usui, K. Kuroki, R. Arita, and H. Aoki, Phys. Rev. Lett. **105**, 057003 (2010).
- [6] Q. Si, R. Yu, and E. Abrahams, Nat. Rev. Mater. **1**, 16017 (2016).
- [7] C. Platt, W. Hanke, and R. Thomale, Adv. Phys. **62**, 453 (2013).
- [8] J. Chaloupka and G. Khaliullin, Phys. Rev. Lett. **100**, 016404 (2008).
- [9] P. Hansmann, X. Yang, A. Toschi, G. Khaliullin, O. K. Andersen, and K. Held, Phys. Rev. Lett. **103**, 016401 (2009).
- [10] G. Zhou, F. Jiang, J. Zang, Z. Quan, and X. Xu, ACS Appl. Mater. Interfaces **10**, 1463 (2018).
- [11] M. J. Han, X. Wang, C. A. Marianetti, and A. J. Millis, Phys. Rev. Lett. **107**, 206804 (2011).
- [12] W. M. Li and al., PNAS **116**, 12156 (2019).
- [13] K. Jiang, X. Wu, J. Hu, and Z. Wang, Phys. Rev. Lett. **121**, 227002 (2018).
- [14] T. Maier, T. Berlijn, and D. J. Scalapino, Phys. Rev. B **99**, 224515 (2019).
- [15] X. Wu, D. Di Sante, T. Schwemmer, W. Hanke, H. Y. Hwang, S. Raghu, and R. Thomale, Phys. Rev. B **101**, 060504(R) (2020).
- [16] D. Li, K. Lee, B. Wang, M. Osada, S. Crossley, H. Lee, Y. Cui, Y. Hikita, and H. Hwang, Nature **572**, 624 (2019).
- [17] W. Kohn and J. M. Luttinger, Phys. Rev. Lett. **15**, 524 (1965).
- [18] S. Raghu, S. A. Kivelson, and D. J. Scalapino, Phys. Rev. B **81**, 224505 (2010).
- [19] W. Metzner, M. Salmhofer, C. Honerkamp, V. Meden,

- and K. Schönhammer, *Rev. Mod. Phys.* **84**, 299 (2012).
- [20] N. F. Berk and J. R. Schrieffer, *Phys. Rev. Lett.* **17**, 433 (1966).
- [21] D. J. Scalapino, E. Loh, and J. E. Hirsch, *Phys. Rev. B* **34**, 8190 (1986).
- [22] S. Graser, T. A. Maier, P. J. Hirschfeld, and D. J. Scalapino, *New Journal of Physics* **11**, 025016 (2009).
- [23] P. Giannozzi and al., *J. Phys.: Cond. Matt.* **21**, 395502 (2009).
- [24] P. Giannozzi and al., *J. Phys.: Cond. Matt.* **29**, 465901 (2017).
- [25] N. Marzari, A. A. Mostofi, J. R. Yates, I. Souza, and D. Vanderbilt, *Rev. Mod. Phys.* **84**, 1419 (2012).
- [26] J. Kanamori, *Prog. Theor. Phys.* **30**, 275 (1963).
- [27] B. Brandow, *Adv. Phys.* **26**, 651 (1977).
- [28] C. Platt, R. Thomale, and W. Hanke, *Phys. Rev. B* **84**, 235121 (2011).
- [29] R. Shankar, *J. Stat. Phys.* **103**, 485 (2001).
- [30] www.gauss-centre.eu.
- [31] www.lrz.de.
- [32] J. P. Perdew, K. Burke, and M. Ernzerhof, *Phys. Rev. Lett.* **77**, 3865 (1996).
- [33] M. Altmeyer, D. Guterding, P. J. Hirschfeld, T. A. Maier, R. Valentí, and D. J. Scalapino, *Phys. Rev. B* **94**, 214515 (2016).
- [34] M. Salmhofer and C. Honerkamp, *Progress of Theoretical Physics* **105**, 1 (2001).
- [35] F. J. Wegner and A. Houghton, *Phys. Rev. A* **8**, 401 (1973).
- [36] J. Polchinski, *Nucl. Phys. B* **231**, 269 (1984).
- [37] C. Wetterich, *Phys. Ref. Lett. B* **301**, 90 (1993).
- [38] T. Takimoto, T. Hotta, and K. Ueda, *Phys. Rev. B* **69**, 104504 (2004).
- [39] K. Kubo, *Phys. Rev. B* **75**, 224509 (2007).
- [40] S. Graser, T. A. Maier, P. J. Hirschfeld, and D. J. Scalapino, *New J. Phys.* **11**, 025016 (2009).
- [41] A. F. Kemper, T. A. Maier, S. Graser, H.-P. Cheng, P. J. Hirschfeld, and D. J. Scalapino, *New J. Phys.* **12**, 073030 (2010).
- [42] S. Raghu and S. A. Kivelson, *Phys. Rev. B* **83**, 094518 (2011).
- [43] S. Raghu, E. Berg, A. V. Chubukov, and S. A. Kivelson, *Phys. Rev. B* **85**, 024516 (2012).
- [44] W. Cho, R. Thomale, S. Raghu, and S. A. Kivelson, *Phys. Rev. B* **88**, 064505 (2013).
- [45] S. Wolf, T. L. Schmidt, and S. Rachel, *Phys. Rev. B* **98**, 174515 (2018).
- [46] S. Wolf and S. Rachel, *Phys. Rev. B* **102**, 174512 (2020).
- [47] R. Shankar, *Rev. Mod. Phys.* **66**, 129 (1994).